IIETA International Information and Engineering Technology Association
Advancing the World of Information and Engineering

Revue des Composites et des Matériaux Avancés-Journal of Composite and Advanced Materials
Vol. 35, No. 3, June, 2025, pp. 413-426
Journal homepage: http://iieta.org/journals/rcma

Numerical and Experimental Study of Coupling Beams in Reinforced Concrete Shear Walls with Diagonal Steel Members

Ali Murtadha Ali*, Bahman Farahmand Azar, Ali Hadidi, Masood Farzam

Department of Civil Engineering, University of Tabriz, Tabriz 51368, Iran

Corresponding Author Email: Ali.m.a@Tabrizu.ac.ir

https://doi.org/10.18280/rcma.350303

Received: 24 April 2025
Revised: 26 May 2025
Accepted: 2 June 2025
Available online: 30 June 2025

Keywords:
coupling beams, cyclic stress, shear walls, diagonal steel member, high-rise buildings

ABSTRACT

The seismic performance of coupling beams in reinforced concrete shear walls is a critical factor in ensuring the safety and resilience of high-rise buildings, particularly in earthquake-prone regions. According to ACI 318, diagonally reinforced coupling beams are designed to deliver superior seismic performance, including ductility and energy dissipation. However, the intricate layout and congestion of diagonal reinforcement pose significant challenges during construction. To address these issues, this study proposes a new type of reinforcement approach—Equivalent Diagonal Reinforcement (EDR)—utilizing diagonal steel elements (DSE) in the form of L- and box-shaped profiles. This study involves both analytical and experimental investigations on three coupling models: one with conventional diagonal reinforcement in accordance with ACI 318 (DRAC) and two, incorporating the proposed EDR system. The EDR-based models use diagonal steel elements in either box-shaped or L-shaped profiles. Experimental and numerical approaches were utilized to assess the seismic behavior of the coupling beams. Cyclic loading tests were conducted to analyze crack propagation, failure modes, and energy absorption, while finite element simulations using ABAQUS/CAE 2022 were employed to validate the experimental findings and provide further insights into stress distribution and post-peak behavior. The findings demonstrate that the proposed EDR system with diagonal steel elements effectively addresses reinforcement congestion issues while achieving desirable performance in terms of stiffness degradation, energy dissipation, and ductility improvement. This study suggests that EDR can serve as a viable alternative to conventional diagonal reinforcement, enhancing both constructability and structural performance.

1. INTRODUCTION

The analysis of structures under seismic loading highlights that collapse is often initiated by the failure of critical components rather than the entire structure [1]. This localized damage is particularly concerning in cast-in-place reinforced concrete structures, where the repair or replacement of damaged components can be costly and, in some cases, impossible [2]. Among these critical elements, coupling beams in reinforced concrete coupled shear walls play a crucial role in resisting lateral forces in high- rise structures. However, due to their low span-to-depth ratios, these beams are highly susceptible to shear failure during significant seismic events [3, 4]. In other words, traditional coupling beams often experience severe damage at their ends, making post-earthquake repair highly challenging [5-8].

Several reinforcement schemes have been suggested to improve the seismic resistance of reinforced concrete coupling beams: rhombic reinforcement and diagonal reinforcement [9, 10]. Although they remain restricted by the limited shear force transmission capabilities of reinforcing steel, especially in beams with low span-to-depth proportions, these layouts greatly increase shear strength and ductility. Shear failure is therefore still the principal kind of failure, usually resulting in a very constricted hysteresis curve. The complexity of reinforcement detailing and the challenges associated with the design, construction, and performance of such beams have motivated researchers to explore alternative reinforcement strategies and innovative structural solutions.

One such substitute for conventional reinforced concrete beams is steel coupling beams. Introduced to increase the seismic performance of linked wall systems, replaceable steel coupling beams provide better reparability [11, 12]. However, problems such as web buckling and concrete crushing at beam-wall interfaces need careful design considerations, especially for web stiffeners and embedment zones to avoid early failures [13].

A notable recent advancement is the concept of replaceable coupling beams (RCBs), where deliberately designed vulnerable sections act as energy-dissipating "fuses" [14-16]. This design allows the beam to undergo plastic deformation while protecting the rest of the structure. The first implementation of RCBs in coupled shear walls introduced a three-segment beam configuration, where the central "fuse"

portion dissipates energy through shear yielding while the end sections remain elastic [17]. Experimental investigations have confirmed that damage is concentrated within the replaceable segment, allowing for easy post-earthquake replacement. Additionally, researchers have explored alternative RCB designs, such as steel truss coupling beams with replaceable buckling-restrained web elements. These systems dissipate energy through shear deformation while being encased in reinforced concrete panels to mitigate out-of-plane buckling effects [18]. The results from cyclic loading tests indicate that such systems exhibit excellent deformation and energy absorption characteristics, with plastic deformation localized within the steel webs. There is also research efforts aimed at reducing seismic response and minimizing damage to coupling beams in shear walls by installing metal rubber (MR) dampers in the coupling beams [19, 20].

Further refinements to RCBs have included variations in fuse configurations, such as steel shear links that connect to beam segments via bolted or welded connections. Studies show that end plate connections are most effective for post-damage repairability, whereas bolted web connections allow for greater residual deformation accommodation. Despite substantial advances in replaceable coupling beams (RCBs), earlier research has concentrated on their component-level behavior and little analysis of their integration into structural systems. Numerous research [21-23] have studied RCB material characteristics, reinforcement configurations, and localized failure processes under cyclic loads. The interaction of these beams with surrounding shear walls, load transfer processes, and structural reaction are understudied. Steel-encased RCBs have improved fracture resistance and ductility, but their performance in a linked shear wall system under seismic excitation needs additional study. Fiber- reinforced polymer (FRP) composite RCBs have shown promise in reducing reinforcement congestion and improving long-term durability, but their effects on global deformation, energy dissipation, and lateral stability are unknown. Optimizing the design, structural integrity, and seismic resilience of high- rise structures requires a full study of RCBs within entire reinforced concrete shear wall systems [24].

While numerous studies [25-27] have examined coupling beam innovations and steel plate- concrete composite shear walls, research on composite coupled shear walls remains relatively scarce.

Previous experimental studies on hybrid coupled shear walls have identified optimal coupling ratios for different wall configurations [28]. Performance-based plastic design methodologies have also been introduced, enabling more efficient energy dissipation in hybrid coupled shear walls. Additionally, novel reinforced concrete linked shear wall designs incorporating replaceable coupling beams and optimized corner components have demonstrated enhanced earthquake resistance when compared to conventional reinforced concrete coupled shear walls [29]. Additionally, researchers have investigated the integration of Engineered Cementitious Composites (ECC) in coupled shear walls, demonstrating significant improvements in crack resistance and post-earthquake reparability Wani et al. [30] and Rashid et al. [31].

This study aims to experimentally and numerically evaluate the seismic performance of reinforced concrete coupling beams using an innovative reinforcement system termed Equivalent Diagonal Reinforcement (EDR), which employs diagonal steel elements in L- and box-shaped profiles. Unlike conventional diagonally reinforced coupling beams as per ACI 318 or contemporary Replaceable Coupling Beams (RCBs), the EDR system addresses a critical gap in constructability and reinforcement congestion without necessitating component replacement post-earthquake. The novelty lies in the conceptual integration of continuous diagonal steel profiles (DSEs) as permanent seismic energy dissipaters within the beam-core, combining the ductility benefits of diagonal rebar with the construction simplicity and modularity of steel elements. While RCB systems typically require complex interface detailing and post-event replacement logistics, the EDR system offers a non-replaceable yet damage-tolerant reinforcement alternative, improving not only energy dissipation and stiffness retention but also reducing cracking and deformation concentration. The study uniquely benchmarks EDR's performance against conventional configurations (DRAC), thus providing new insights into optimizing coupling beam design for seismic resilience in high-rise structures.

2. EXPERIMENTAL STUDY

2.1 Model details and characteristics

Designed with exact dimensions (200×500×1000 mm) and a consistent length-to-depth ratio ($ln/h = 2$), three diagonally reinforced coupling beam specimens were evaluated structurally under seismic stress. Comprising two sets of D18 diagonal bars as the primary reinforcement, limited by D8 stirrups spaced at 80 mm, the first specimen was strengthened following ACI 318 [32] regulations. Instead, the two suggested examples are shown using an Equivalent Diagonal Reinforcement (EDR) scheme, which combines Diagonal Steel Elements (DSE). One example used a Box-shaped profile, while the other included an L-shaped profile, providing a fresh approach to reduce congestion and improve constructability and seismic resistance. Figure 1 shows the reinforcing configurations and model dimensions; Figure 2 shows a general view of the specimens before concrete casting.

2.2 Materials characteristics

The compressive strength of concrete (fc') is 40 MPa. Based on testing a cubic specimen with dimensions of 150*150*150mm, and the concrete mix design was established according to the compressive strength. Strength testing was performed on the concrete specimens for each coupling beam (DRAC) and (EDR). To determine the yield and ultimate stress (DSE) of the specimen used (EDR), ASTM A370-14 was used to create two tiny specimens of each flange, which were then put through tensile testing. Table 1 displays the test results. The yield stresses and ultimate stresses of the Ø25, Ø18, Ø10, and Ø8 ribbed bars used in the specimen were also investigated (DRAC), and the findings are displayed in Table 1.

2.3 Test setup descriptions

The experimental test setup assessed coupling beam specimen performance under lateral cyclic stress. Each sample was positioned vertically and anchored to the laboratory floor using steel beams and twenty-four 25 mm-diameter threaded bars on each side. To accurately immobilize the specimen at

the test configuration point. A small block linked to the horizontal actuator transferred the cyclic load to the specimen. The actuator supplied stress directly to the tiny block and dispersed it via threaded rods to allow back-and-forth movement during testing. Eight 25 mm threaded bars were mounted via a large steel flange portion to join the actuator to the compact block for uniform force transmission. Four side supports were fitted to avoid specimen out-of-plane buckling or lateral movement after loading. These supports were placed on both sides of its plane to stabilize the little block. The Tabriz University Structural Laboratory built and ran the experiment using superior capabilities to assure accuracy and reliability. The rigid floor anchoring, horizontal actuator connection, side supports for stability, and structural arrangement for cyclic loading assessment are shown in Figure 3.

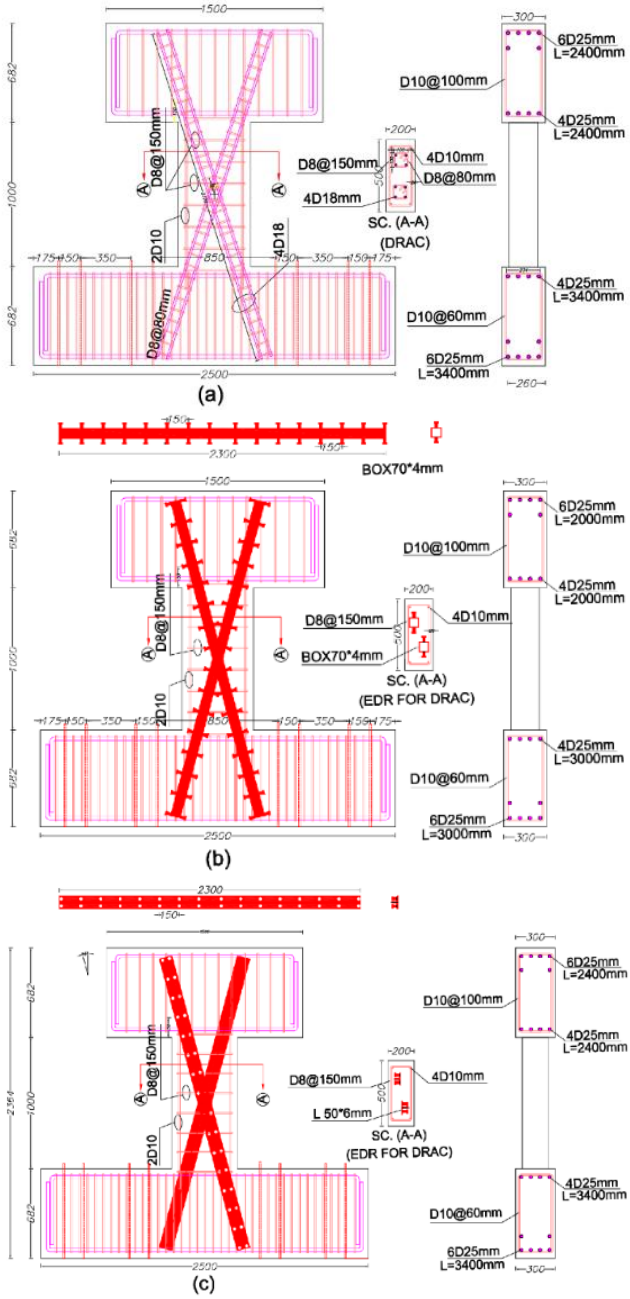

Figure 1. Samples dimensions with reinforcement details for: (a) specimen (DRAC) (b) specimen (Box70) (c) specimen (L50)

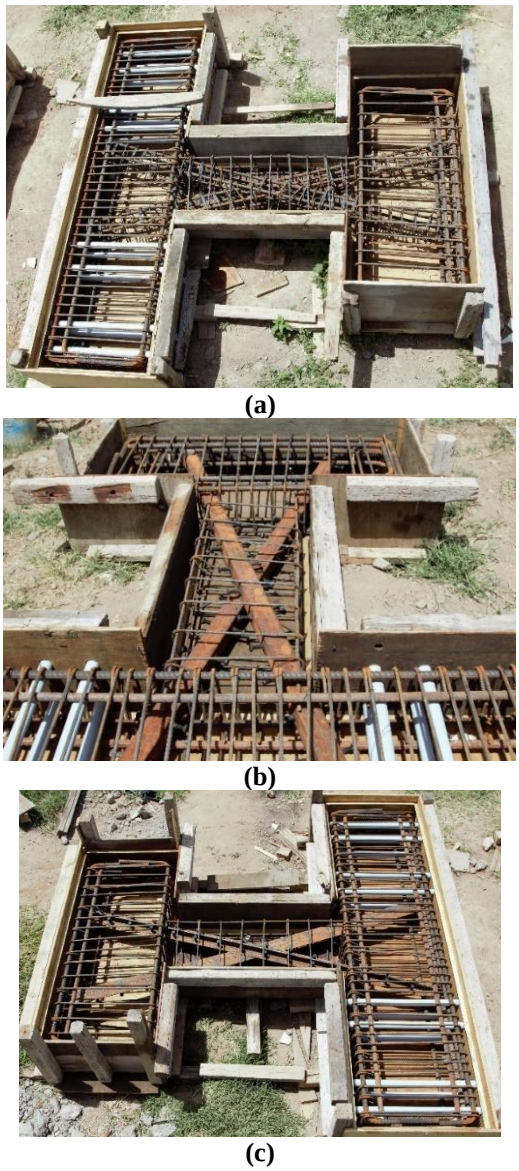

Figure 2. Reinforcement models before pouring concrete (a) sample (DRAC) (b) sample (Box70) (c) sample (L50)

To ensure the accuracy and reliability of the applied loads during cyclic testing, the actuator system underwent a comprehensive calibration process prior to the commencement of experiments. The load cell was verified using a certified calibration block and cross-checked against a known reference weight to confirm linearity and load measurement accuracy within ±1% of full scale. Zero drift correction was performed by resetting the baseline output of both load and displacement sensors before each test cycle to mitigate cumulative error, particularly under long-duration loading. Additionally, the actuator's displacement transducer (LVDT) was calibrated against a precision dial gauge to validate stroke accuracy, with tolerances maintained within ±0.2 mm.

In the experimental setup, the boundary conditions were carefully configured to simulate realistic constraints typically observed in structural wall systems with coupling beams. The specimens were anchored to a rigid steel reaction frame using high-strength threaded rods (25 mm diameter), which were firmly grouted into the concrete blocks at both beam ends to prevent unintended translation or uplift. Lateral and vertical restraints were applied to the supports to restrict movement in all translational directions, ensuring that the imposed

deformations were localized within the coupling beam. To prevent rotational degrees of freedom at the supports, steel plates with welded stiffeners were used in conjunction with torque-controlled anchoring, effectively creating a fixed-end condition.

To assess the consistency and variability of the mechanical properties of reinforcement materials used in the experimental program, a statistical evaluation was conducted on the measured yield strength, tensile strength, and ultimate elongation for all reinforcement types listed in Table 1. The analysis included the calculation of basic descriptive statistics—mean, standard deviation (std), minimum, maximum, and coefficient of variation (COV)—for each property. The mean value was computed to represent the central tendency, while the standard deviation quantified the spread of data around the mean. The coefficient of variation (COV) was expressed as the ratio of the standard deviation to the mean, multiplied by 100%, serving as a normalized measure of dispersion to allow comparison across parameters with different units. In addition, the percent deviation of each specimen's measured yield strength from its nominal (design-specified) value was calculated to evaluate compliance with material specifications. This was defined by the equation:

$$\text{Percent Deviation} = \left(\frac{f_y - f_{y,n}}{f_{y,n}}\right) \times 100 \quad (1)$$

As shown in Table 1, measured yield strengths varied significantly across the tested specimens. While Φ8 reinforcement exhibited no deviation from its nominal value of 300 MPa, higher deviations were observed for other diameters, with Φ10, Φ18, and Φ25 showing yield strength increases of 14%, 51.67%, and 71.33% respectively. Fabricated profiles such as BOX 70×4 mm and L 50×6 mm recorded deviations of 24.17% and 10% from their nominal 240 MPa yield strength, respectively. The statistical summary of the measured yield strength revealed a mean of 362.17 MPa, a standard deviation of 99.7 MPa, and a coefficient of variation (COV) of 25.13%, indicating moderate to high variability across the samples. Similarly, tensile strengths had a mean value of 518.17 MPa with a standard deviation of 111.91 MPa and a COV of 19.71%. The ultimate elongation also showed considerable dispersion, with a mean of 19.24% and a COV of 31.91%. These statistical metrics highlight the inherent material variability and underscore the importance of reporting such data in experimental investigations to support analytical validation, ensure consistency in test comparisons, and reinforce the credibility of derived structural performance conclusions.

As depicted in Figure 4, before pouring concrete for the diagonally reinforced coupling beam (DRAC) specimens, six strain gauges of various rosette types were installed on the steel portions to monitor strain magnitudes. Similarly, six additional strain gauges were installed at the same positions on the diagonal reinforcements of the proposed specimens (Box70 and L50), ensuring uniformity in measuring strain responses in the diagonal, horizontal, and vertical directions. To track displacement under lateral loading, two Linear Variable Differential Transformers (LVDTs) were mounted at the ends of the large block to measure horizontal movement. At the same time, an additional LVDT was placed on top of the block to document vertical displacement. The setup in the image demonstrates the precise placement of strain gauges and LVDTs, providing a comprehensive configuration for assessing strain and movement during cyclic loading tests.

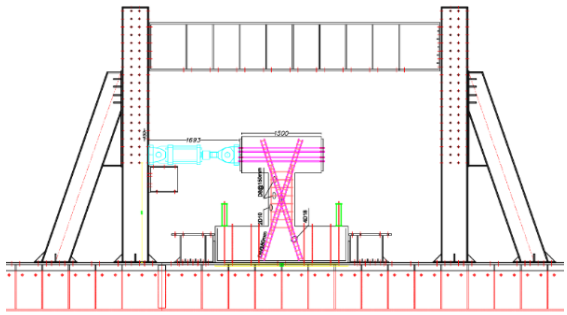

(a)

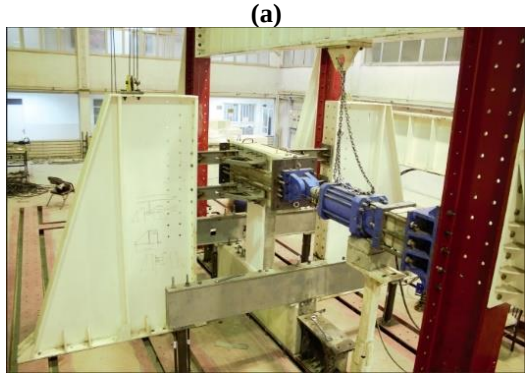

(b)

Figure 3. Set up for testing coupling beam samples: a) sketch of testing device; b) the available testing device in the university laboratory

Table 1. Mechanical features of utilized materials with statistical analysis

Type	Diameter / Thickness (mm)	Nominal Yield Strength $f_{y,n}$ MPa)	Measured Yield Strength f_y (MPa)	Measured Tensile Strength f_u (MPa)	Ultimate Elongation (%)	Percent Deviation
Φ8	8	300	300	494	23	0
Φ10	10	300	342	522	24	14
Φ18	18	300	455	579	27	51.67
Φ25	25	300	514	667	19	71.33
BOX 70*4mm	4	240	298	328	11.42	24.17
L 50*6mm	6	240	264	519	11	10
Statistical Analysis of Material						
mean	-	-	362.17	518.17	19.24	
std	-	-	99.7	111.91	6.72	
min	-	-	264.0	328.0	11.0	
max	-	-	514.0	667.0	27.0	
COV (%)	-	-	25.13	19.71	31.91	

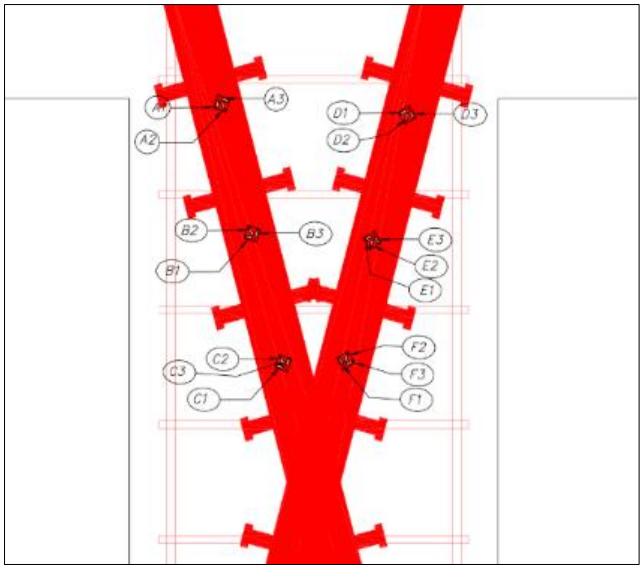

Figure 4. Position of measuring instruments

The cyclic loading protocol adopted in this study was displacement-controlled and designed to reflect the inelastic deformation demands imposed by strong seismic events. The selection of a maximum displacement amplitude of ±80 mm and a total of 45 cycles was guided by established precedents in experimental research on coupling beams and reinforced concrete components subjected to reversed cyclic loading. The procedure closely aligns with the guidelines set forth in ACI 374.1-05 and FEMA 461, which recommend progressively increasing displacement amplitudes to capture elastic, yield, and post-yield behavior. Initial low-amplitude cycles were used to characterize stiffness and elastic response, while subsequent increments targeted the nonlinear range to evaluate damage progression, energy dissipation, and ductility. The symmetric application of loading in both directions allowed for a balanced assessment of tensile and compressive behavior, emulating bidirectional seismic forces. The selected protocol ensured that the specimens were subjected to realistic and comprehensive inelastic deformation histories, capturing key failure modes such as diagonal cracking, bar yielding, and local buckling. Therefore, the loading sequence was appropriately chosen to simulate field-representative cyclic demands and to enable meaningful comparison with prior studies on similar structural elements, as shown in Figure 5.

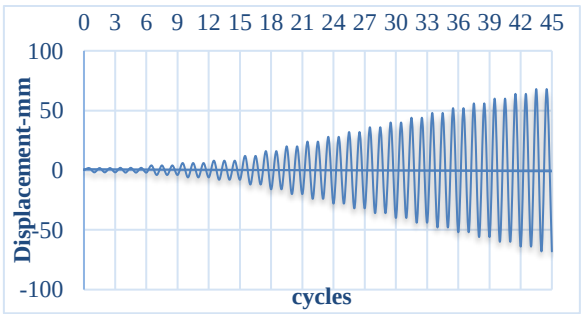

Figure 5. Cyclic loading protocol used for coupling beam samples

2.4 Degradation of structural integrity

The strength degradation ratio (ηi), the greatest strength of the most recent cycle divided by the strength of the initial cycle at the same displacement level, can be utilized to determine the strength degradation, as the relationship below illustrates [33].

$$\eta i = \frac{Fni}{F1i} \tag{2}$$

where, ($F^n{}_i$) is the peak strength in the cycle (n^{th}) at displacement (i^{th}) and (F_1) represents the peak strength in the first cycle at the same displacement.

The stiffness deterioration can be computed using multiple methods. The maximum load of each cycle ($P^i{}_j$) is added for each specific deformation controlled (Δ_j), and the value obtained is divided by the total of the cycle's deformations ($\Delta^i{}_j$) [34]. In this manner, the current stiffness for that particular displacement is attained.

$$K_i = \sum_{i=1}^{n} pij \,/\, \sum_{i=1}^{n} \Delta ij \tag{3}$$

The following relation was utilized to get the stiffness of the walls in each cycle [35].

$$Ki = \frac{[+Pi]-|-Pi|}{|+\Delta i|-|-\Delta i|} \tag{4}$$

Δi shows the same cycle's distortion in positive and negative directions, and ± Pi represents the peak existent strength in the i^{th} cycle.

2.5 Energy dissipation assessment

The equivalent damping coefficient is calculated from the following relationship:

$$\xi eq = \frac{Ah}{2\pi Ae} \tag{5}$$

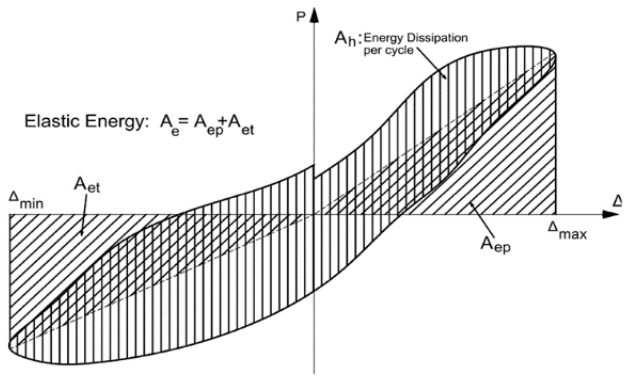

Figure 6. Determining energy dissipation per cycle and elastic energy

Figure 6 illustrates the methodology for calculating the energy dissipation and elastic stress energy within a hysteresis cycle. The enclosed area within the hysteresis loop represents the dissipated energy per cycle (Ah), which quantifies the energy lost due to inelastic deformations. Meanwhile, the elastic stress energy (Ae) is estimated by summing the areas enclosed between each cycle and the horizontal axis in both the positive and negative displacement directions. This provides an assessment of the energy stored in the system at peak displacement before unloading occurs. Figure 7, visually demonstrates these energy components, highlighting the

balance between dissipated and stored energy during cyclic loading.

3. NUMERICAL MODELING

3.1 FEM-Based structural simulation

To predict structural behavior under varying load loops and deformations, FEM-based numerical models were developed in ABAQUS/CAE 2022. These models were meticulously constructed to validate and complement experimental results, employing eight-node brick elements (C3D8R) with three translational degrees of freedom per node for all steel and concrete components, including studs, profiles, and steel sections. A 2-node truss element (T3D2) with similar translational degrees of freedom was also used to model encased reinforcing steel. To ensure analysis accuracy and convergence, the maximum element mesh size was limited to 50 mm, with finer meshes of 5 mm applied to bolt elements due to their small diameter (10 mm) and cylindrical geometry. For steel profiles, the mesh size was refined to 3 mm along the web plane thickness and flange extensions, significantly enhancing the convergence of the finite element (FE) analysis. The dimensions of the numerical models were aligned with experimental counterparts, as shown in Figure 7, featuring interlocking steel elements for Box70 and L50 specimens. Under established protocols, cyclic loads were applied to the upper block, and corresponding load responses were extracted for analysis. Beam degrees of freedom were restricted to rotation and planar translation around a vertical axis perpendicular to the plane. At the same time, translational constraints along three principal axes accounted for the foundation's outer planes. For reinforced steel and element-to-element interactions, tie constraints were employed, ensuring compatibility between reinforcement and surrounding concrete through embedded region interaction. This modeling approach guaranteed that the reinforcement strain remained consistent with the concrete's, accurately simulating structural behavior.

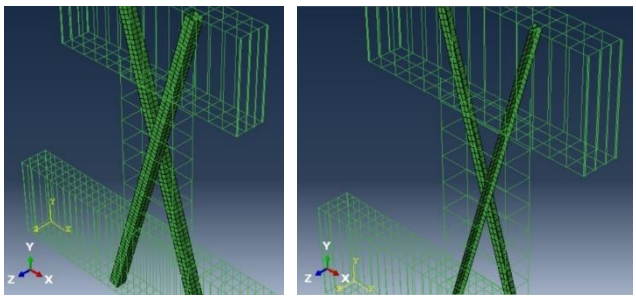

Figure 7. Mesh creation in the samples (a) Box70 (b) L50 for various steel element kinds

3.2 Material characteristics

3.2.1 Modeling concrete behavior

The study utilizes Finite Element Analysis (FEA) to simulate the nonlinear cyclic response of reinforced concrete members through the application of the Concrete Damaged Plasticity (CDP) model within the ABAQUS platform. Recognized for its ability to represent quasi-brittle failure mechanisms, the CDP model enables the incorporation of key behavioral phenomena such as stiffness degradation and irreversible strain accumulation. It achieves this by employing a continuum damage framework that combines compressive crushing and tensile cracking in an isotropic plasticity formulation. For implementation, the model requires the definition of stress-strain responses under uniaxial tension and compression, which are characterized by an initial elastic regime followed by progressive inelastic softening beyond the tensile and compressive yield thresholds (σt0 and σc0). These relationships, presented in Figure 8, were defined using parameters such as initial elastic modulus (E0), peak strengths, and corresponding strains (εt and εc), providing the foundation for capturing nonlinear concrete behavior.

While the numerical results closely aligned with experimental data in terms of maximum load resistance and elastic stiffness, notable divergence was observed in the softening phase, particularly for the L50 configuration. This discrepancy can be linked to the simplifications intrinsic to the CDP model, including its uniform treatment of damage in tension and compression, which may not fully reflect the directional dependency of cracking or the localized failure zones typical in coupling beams. Additionally, the model's post-peak accuracy is highly dependent on parameter calibration, as factors such as the dilation angle, viscosity coefficient, and damage evolution laws significantly influence the shape of the descending branch. Without precise experimental calibration, these inputs can yield artificially stiff or delayed responses, thus limiting the model's predictive capacity for advanced cyclic degradation and energy dissipation characteristics [36].

$$\sigma c = (1 - dc)E0\,(\,\varepsilon c - \varepsilon plc\,) \quad (6)$$

$$\sigma t = (1 - dt)E0\,(\,\varepsilon t - \varepsilon plt\,) \quad (7)$$

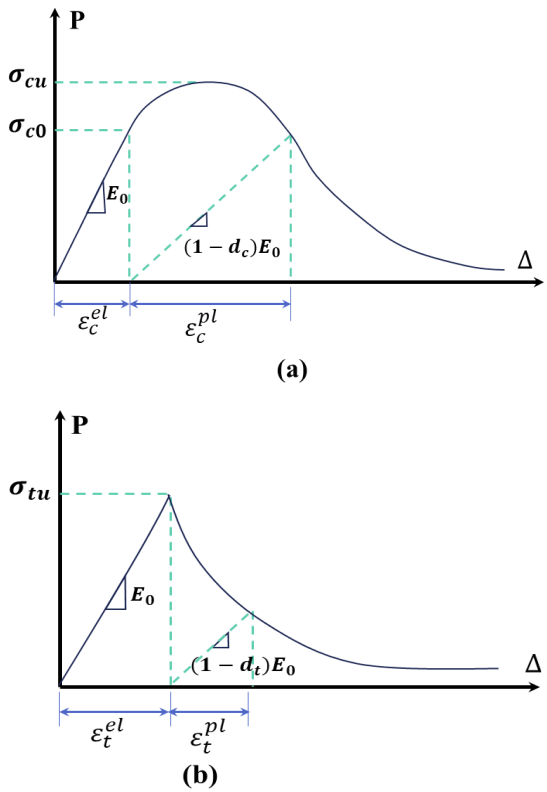

Figure 8. Concrete typical behaviour: a) in uniaxial compression and b) in uniaxial tension

Table 2. CDP variables for ABAQUS material definition of concrete

Parameter	Taken Value	Description
Ψ	30	Dilation angle
e	0.1	Eccentricity
f_{b0}/f_{c0}	1.16	Initial uniaxial compressive yield stress divided by starting equibiaxial compressive yield stress.
K	0.6667	KC, the proportion of the second stress invariant on the tensile meridian.
M	0.0001	Viscosity parameter

In this case, the parameters that affect the compressive and tensile damage indices—compressive and tensile strength, plastic compressive strain, plastic tensile strain, and temperature are represented by the letter's dc and dt, respectively. These numbers range from 0 to 1. Various relationships have been recommended to determine these parameters, generally depending on the formulas recommended by Dong et al. [37]. The concrete behavior of the concrete was modeled using the constitutive model of concrete damage plasticity in ABAQUS. in Table 2. The ABAQUS user manual includes more comprehensive details about CDP settings [38, 39].

3.2.2 Steel modeling

The steel's behavior was modeled using a bilinear curve, and isometric hardening has been considered as well. The Poisson's proportion for the steel material model was set at 0.3. The coupon tensile strength test found the modulus of elasticity, matching elongation value (εn), and tensile strength value (Fy) of the reinforcing bars and profiles.

4. RESULTS AND DISCUSSION

4.1 Experimental results

4.1.1 Cracks patterns

The fracture mechanisms across all specimens were similar, involving shear and flexural failures, but differences in crack patterns and progression were observed during cyclic loading. In the Box70 sample, initial cracks appeared during the second cyclic loading ring, forming in the middle of the model at a 45-degree angle. These cracks extended toward the bottom and top of the sample at the same angle, reaching the 17th loading cycle (Figure 9a). By the 18th cycle, the yielding state was exceeded, with horizontal cracks spreading over a broader area and growing significantly. Spalling was noted in the 26th cycle (Figure 9b), while twisting of the longitudinal bars began in the 31st cycle, leading to their breakage in the 36th cycle (Figure 9c). Despite the damage, the diagonal steel elements in the design ensured structural stability, preventing collapse until the test concluded.

In the L50 sample, cracks also initiated during the second cyclic loading ring at a 45-degree angle in the middle of the model and extended upward and downward, reaching the 17th cycle (Figure 10a). Yielding occurred in the 18th cycle, followed by extensive horizontal cracking and spalling by the 31st cycle (Figure 10b). Twisting of the longitudinal bars started in the 32nd cycle, culminating in their breakage in the 36th cycle (Figure 10c). The inclined steel elements provided sufficient reinforcement to maintain the sample's stability throughout the loading process, preventing complete failure.

(a) **(b)** **(c)**

Figure 9. Stages of cracking and fracture in sample Box 70

(a) **(b)** **(c)**

Figure 10. Stages of cracking and fracture in sample L50

Similarly, in the DRAC sample, cracks first appeared in the second cyclic loading ring at a 45-degree angle at the model's center. They propagated toward the top and bottom by the 17th cycle (Figure 11a). The 18th cycle marked the yielding state with horizontal cracks expanding further. Spalling of the concrete cover occurred by the 31st cycle (Figure 11b), and the longitudinal bars began to buckle in the 32nd cycle, eventually breaking during the 36th cycle (Figure 11c). The diagonal reinforcement maintained structural integrity, preventing collapse until the test's completion.

The findings highlight the significant contribution of diagonal steel elements and reinforcement in enhancing the deformation capacity and stability of the specimens. The Box70 and L50 designs demonstrated superior resistance to crack propagation and collapse compared to the conventional DRAC sample, emphasizing the effectiveness of the proposed reinforcement systems. The figures referenced provide clear visual evidence of the crack evolution and failure mechanisms during testing.

(a) **(b)** **(c)**

Figure 11. Stages of cracking and fracture in sample DRAC

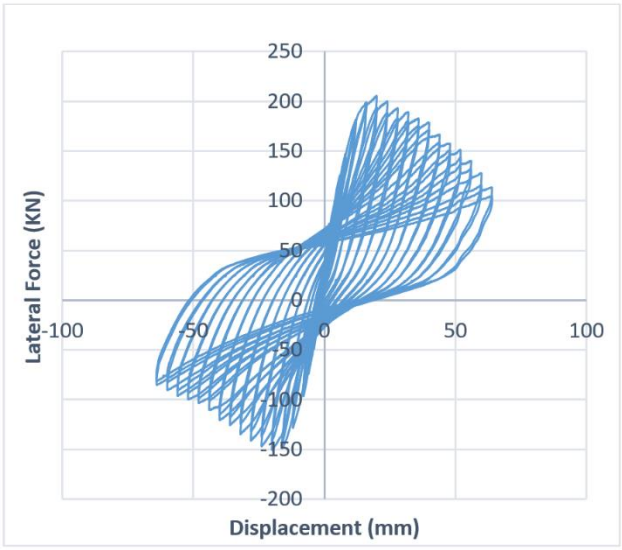

(a)

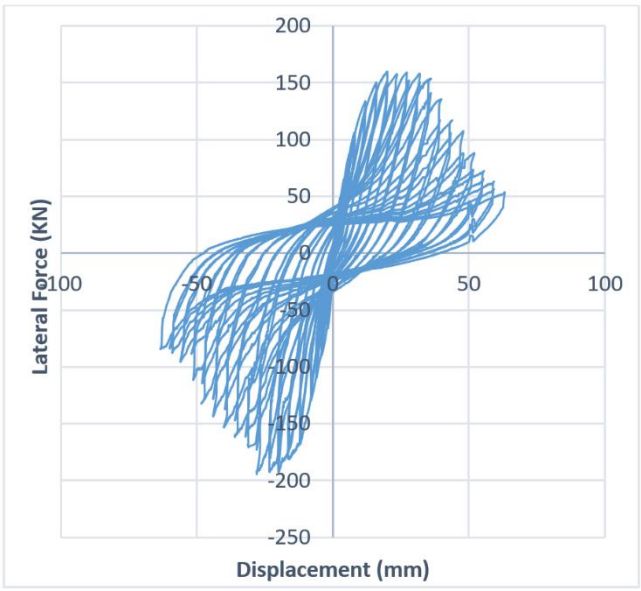

(b)

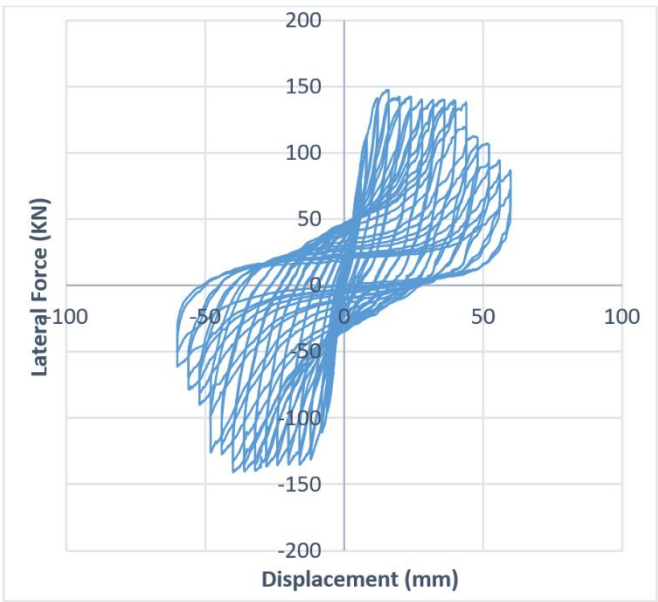

(c)

Figure 12. Lateral force versus displacement hysteretic curves: a) Experimental DRAC; b) Experimental Box 70; c) Experimental L50

4.1.2 Diagram of a hysteretic cycle

Figure 12 demonstrates the lateral force against displacement hysteretic curves for (DRAC), (Box70), and (L50), respectively. Which show symmetrical behavior in the positive and negative displacement areas, indicating balanced responses under cyclic loading. The DRAC and L50 specimens had the broadest hysteretic loops, indicating improved energy dissipation and ductility, which dispersed stresses and withstood lateral forces. The Box70 specimen's hysteretic curve is thinner, showing less energy dissipation due to the lack of concrete infill, which hindered its ability to absorb and store energy during cyclic deformation. However, Box70's stiff box-shaped diagonal steel components provided adequate ductility and structural stability.

In Figure 13, we notice the backbone curves and we obtain it by connecting the peak points for each cycle at each displacement level. The yield points and the ultimate point (failure) for the samples were also determined on the backbone curves.

4.2 Degradation of strength and stiffness

Figure 14 shows the strength degradation ratio for DRAC, Box70, and L50 coupling beam specimens under cyclic loading, showing their ability to sustain load-carrying capability as deformation rises. At the start of the experiment, the DRAC sample experienced a significant loss in stiffness compared to the L50 and Box70 samples, which did not experience a substantial loss in stiffness but retained their strengths. Pre-yield, the strength degradation ratio (ηi) varied from 0.90 to 0.98, showing efficient performance across all specimens. L-shaped diagonal steel parts improve load distribution and postpone significant strength loss, allowing the L50 specimen to demonstrate modest strength deterioration at higher displacements. Overall, Box70 lost more strength beyond the yield point than L50, which lost more than DRAC.

The observed 23.28% increase in peak load capacity for the L50 specimen relative to the conventional DRAC configuration highlights the structural advantage of incorporating L-shaped steel profiles as equivalent diagonal reinforcement. However, for broader applicability and practical implementation in seismic design, it is essential to contextualize this enhancement against constructability and economic trade-offs. While the L50 system offers improved energy dissipation and stiffness retention under cyclic loading, its use introduces additional fabrication steps, including precise cutting, welding, and anchorage detailing for the diagonal steel sections. These requirements may increase initial construction complexity and labor demands compared to traditional rebar-based detailing. Moreover, material costs for L-shaped profiles are generally higher per unit mass than standard reinforcing bars, and site handling may be less flexible due to their non-deformable geometry.

Figure 15 shows the stiffness degradation due to deformation in the positive and negative directions of the specimens. According to the schematic diagram, DRAC, Box70, and L50 coupling beam specimens preserve stiffness as displacement increases, where the stiffness degradation in the positive direction of the specimen (DRAC) was less than that of the specimens (Box70 and L50). In the negative direction, specimen (Box70) was less than that of specimens (DRAC and L50) during the entire loading process. The stiffness degradation trend of the specimens was generally

similar, as shown in Table 3.

To compare the amount of Stiffness degradation of the samples, it can use the graph in Figure 16 to determine the initial Stiffness values (Ko), yield Stiffness values (Ky), peak secant Stiffness (Kmax), and extract the Stiffness degradation coefficients (β1, β2). Where (K_o corresponds to Δ_{cr}) in the second cycle in all samples, and (K_y corresponds to Δ_y) and (K_{max} corresponds to Δ_{max}) in all samples as listed in Table 4.

We note from Figure 16 and Table 4 that the initial stiffness (K_0) of sample (L50) is 44.34% less than that of sample (DRAC), whereas the stiffness of yield stiffness (K_y) and peak secant stiffness (K_{max}) is almost equal. We note from this and from the graph as well that sample (L50) has less than the other two samples, especially at the beginning of the experiment. Therefore, the stiffness degradation coefficient (β1, β2) of sample (L50) increased by (68.62%, and 80%) respectively, compared to sample (DRAC). It was also found that the stiffness degradation coefficient (β1, β2) of the sample (DRAC) was higher by (18.60%, 12.90%), respectively, compared to the sample (Box70).

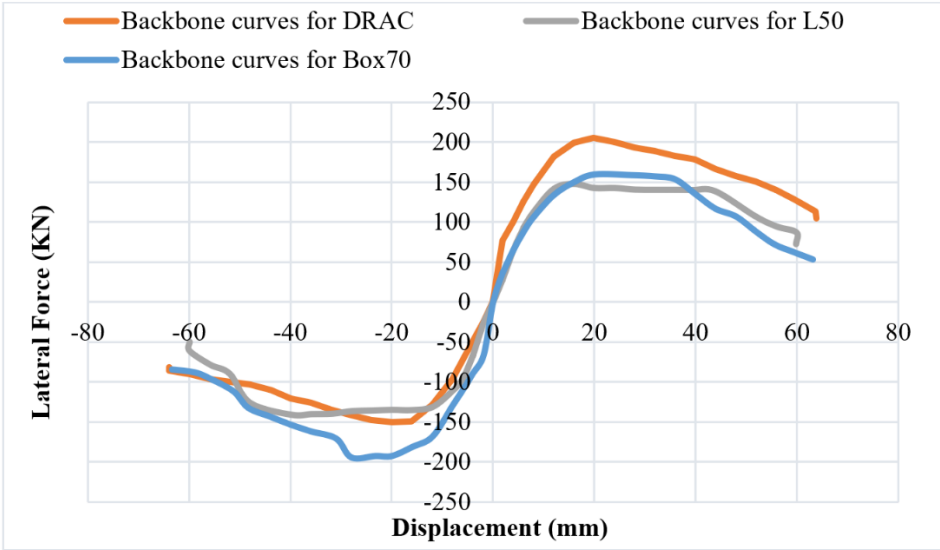

Figure 13. Comparison of Backbone curves of three specimens

Table 3. Load carrying capacity, deformation capacity in various conditions, and coefficient of ductility

Specimen	Loading Direction	Initial Cracking Point		Yield Point		Peak Strength Point		Ultimate Point		Ductility Coefficient
		F_{cr} (KN)	Δcr (mm)	F_y (KN)	Δ_y (mm)	Fmax (KN)	Δmax (mm)	F_u (KN)	Δ_u (mm)	μ
DRAC	Pos. direction	71.82	1.73	161.12	9.63	205.62	19.88	164.5	44.85	3.85
	Neg. direction	-17.29	-1.77	-130.35	-12.35	-150.56	-19.96	-120.44	-39.93	
Box70	Pos. direction	35.38	1.82	130.37	11.44	159.87	20.02	127.89	41.55	3.56
	Neg. direction	-63.04	-1.82	-160.2	-11.13	-194.45	-27.99	-155.55	-38.91	
L50	Pos. direction	27.93	1.84	123.52	9.5	147.63	15.91	118.1	48.98	5.4
	Neg. direction	-24.21	-1.82	-114.54	-8.7	-140.98	-39.88	-112.78	-49.46	

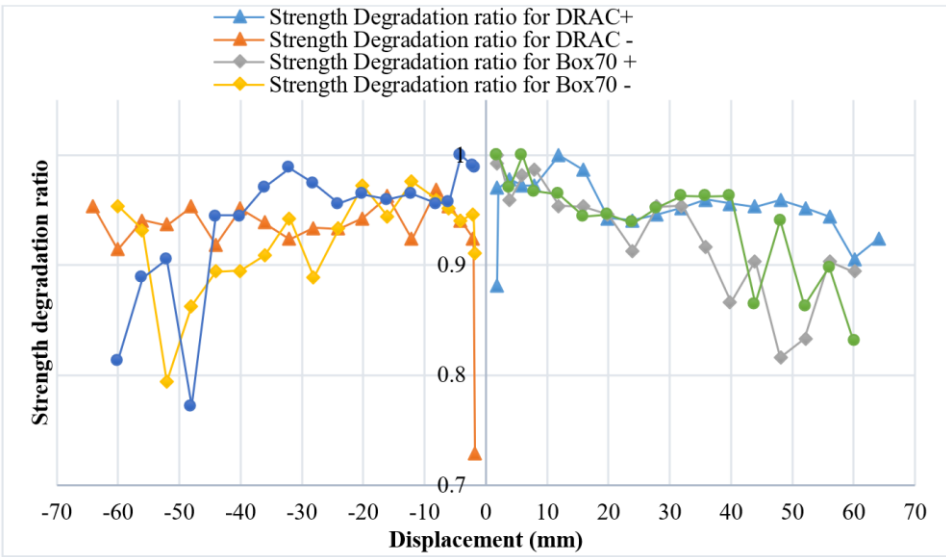

Figure 14. Strength degradation ratio for deformation for three specimens

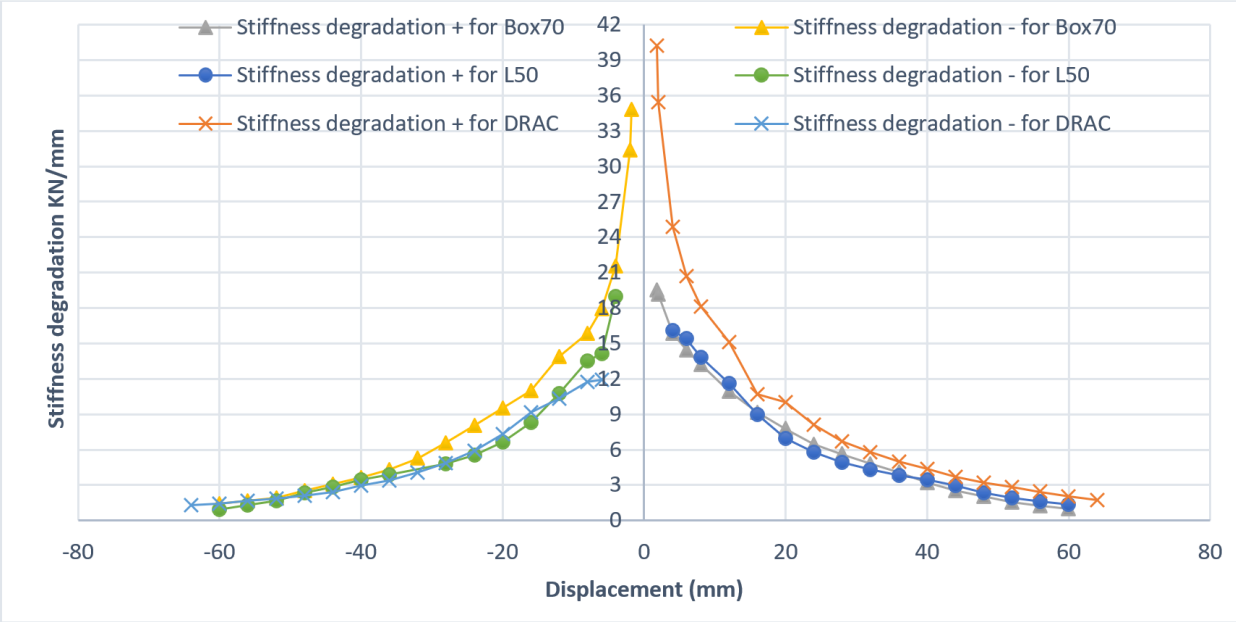

Figure 15. Degradation of stiffness for both positive and negative deformation

Table 4. The specimens' stiffness degradation coefficient

Specimen	Initial Stiffness K_0 (KN/mm)	Yield Stiffness K_y (KN/mm)	Secant peak stiffness K_{max} (KN/mm)	$\beta 1 = K_y/K_0$	$\beta 2 = K_{max}/K_0$
DRAC	25.46	13.01	9.00	0.51	0.35
Box70	27.04	11.63	8.48	0.43	0.31
L50	14.17	12.21	8.91	0.86	0.63

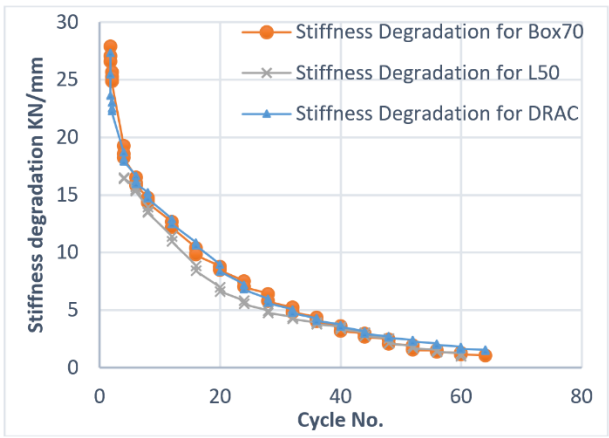

Figure 16. Stiffness degradation per cycle in the three specimens

4.3 Energy dissipation

The three coupling beam specimens—DRAC, L50, and Box70—show their energy absorption and dissipation capabilities under cyclic loading in Figure 17. The L50 specimen has the most significant cumulative dissipated energy at the ultimate point, about (81.30 kN.m). Effective stress distribution and delayed deterioration maximize energy dissipation throughout loading cycles. The cumulative dissipated energy was lower for the DRAC specimen (59.13 KN.m) than for the L50 specimen at the ultimate point. Box70 specimen had the lowest cumulative dissipated energy at the ultimate point (50.66 kN.m) owing to a lack of concrete filling, limiting its capacity to absorb and dissipate energy under cyclic loading. Its slower energy buildup rate makes Box70 less seismically resilient.

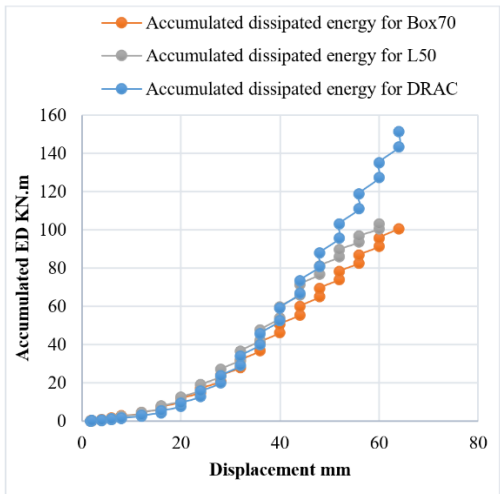

Figure 17. Variation of accumulated dissipated energy with displacement for the three specimens

Figure 18 shows the damping coefficient (ξ) fluctuation for DRAC, L50, and Box70 specimens under cyclic loading, demonstrating energy dissipation during multiple deformations. (L50) has the most significant and stable damping coefficient at the peak point (Δmax), which is greater than that of a sample (Box70) by (19.64%) and (31.37%) greater than that of the (DRAC), dissipating energy well and providing stress redistribution and structural integrity under cyclic pressures. As for the sample (Box70), it was greater

than the (DRAC) coefficient by (9.80%). This indicates that its lack of concrete filling limits its energy dissipation capability and structural stability.

To evaluate the energy dissipation capacity of the tested coupling beams, the equivalent viscous damping ratio (ξ) was computed at various drift levels and plotted in Figure 19. According to ASCE 7, a typical damping ratio of 5% of critical damping is assumed for seismic design of conventional structures. In this context, the damping ratios at peak point recorded for the DRAC, BOX70, and L50 specimens were 5.0%, 5.5%, and 6.0%, respectively. Both the BOX70 and L50 specimens exceeded the standard 5% threshold, indicating enhanced energy dissipation characteristics. This elevated damping performance suggests that coupling beams incorporating equivalent diagonal reinforcement (EDR), particularly the L50 configuration, are more effective in absorbing seismic input energy. As a result, such configurations can reduce the amplitude of seismic forces transmitted to the surrounding structural elements, potentially enhancing global seismic performance and reducing inelastic demand on the structural system. These findings support the viability of EDR-based coupling beams as energy-dissipative components in seismic design frameworks, warranting further integration into performance-based design strategies.

4.4 Findings from finite element analysis

The finite element simulations conducted within the scope of this investigation exhibited a satisfactory correlation with the experimental results in terms of initial stiffness, peak load resistance, and the overall hysteretic response envelope. Nevertheless, discernible deviations were observed during the post-peak phase, particularly for the Box70 and L50 configurations, where the numerical models underpredicted the rate of stiffness degradation and energy dissipation capacity under reversed cyclic loading. These discrepancies are primarily attributed to the inherent limitations of the Concrete Damaged Plasticity (CDP) constitutive model in accurately capturing localized fracture mechanisms, progressive cyclic deterioration, and the nonlinear interaction between the reinforcing steel and the surrounding concrete matrix under large inelastic excursions. The predictive accuracy of the CDP framework is highly sensitive to the definition of key material parameters, including the dilation angle, compressive and tensile damage evolution laws, and fracture energy values. Inadequate calibration of these parameters, especially in the context of non-standard reinforcement geometries and complex stress distributions, may result in numerical artifacts and misrepresentation of the structural softening behavior. Further refinement of the damage modeling parameters, informed by experimental data and localized strain measurements, is essential to enhance the reliability of post-peak response simulations.

Figure 19 illustrates the comparison between the experimental backbone diagrams and finite element (FE) analysis results for the DRAC, Box70, and L50 specimens, demonstrating the ability of the FE models to replicate the structural behavior under cyclic loading. For the DRAC specimen, the FE analysis closely mirrors the experimental findings, particularly in capturing the initial stiffness, yielding behavior, and peak lateral force, which can be attributed to the accurate modeling of the robust diagonal reinforcement and its effective stress redistribution capabilities. The Box70 specimen also shows good alignment between the FE analysis and experimental data in the early loading stages and peak strength region; however, the FE model underestimates the steep decline in lateral force observed experimentally in the post-peak phase, likely due to the absence of concrete infill, which introduces complex failure mechanisms not fully captured numerically. In the L50 specimen, the FE model provides reasonable predictions for the initial stiffness and peak strength. However, deviations arise in the post-peak phase, where the analysis overestimates the lateral force at larger displacements, resulting from the simplified representation of the L-shaped reinforcement, which does not fully account for material degradation and localized stress redistribution.

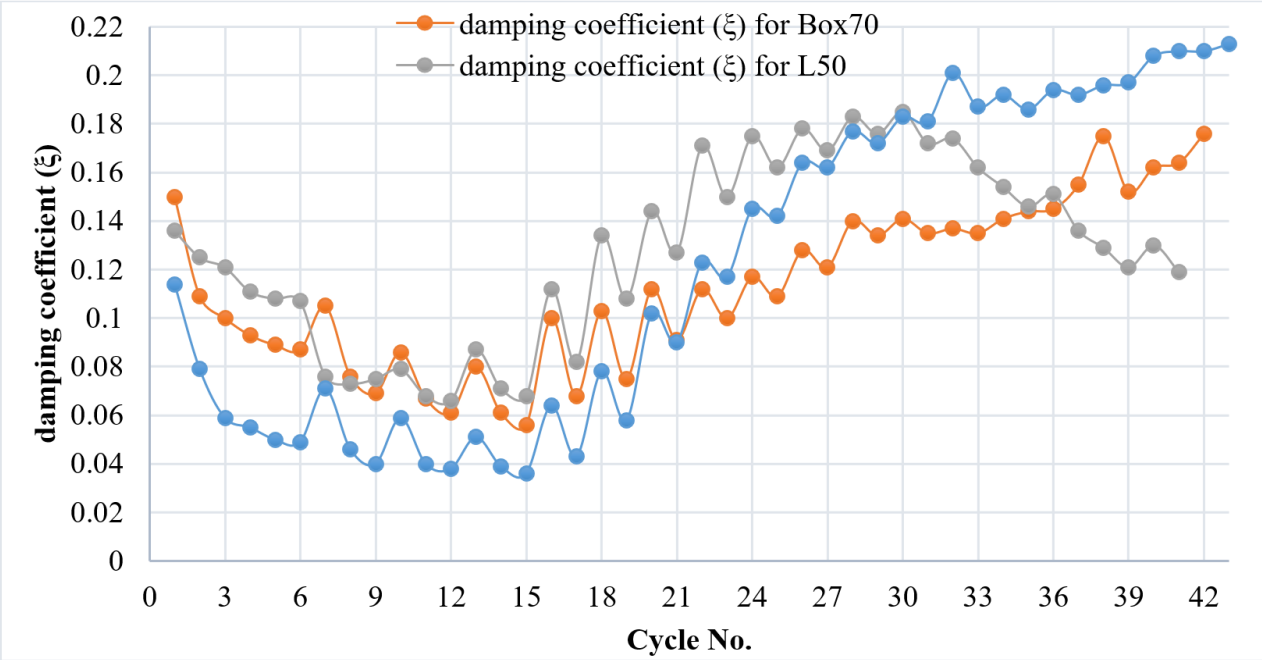

Figure 18. Damping coefficient for the three samples throughout various cycles

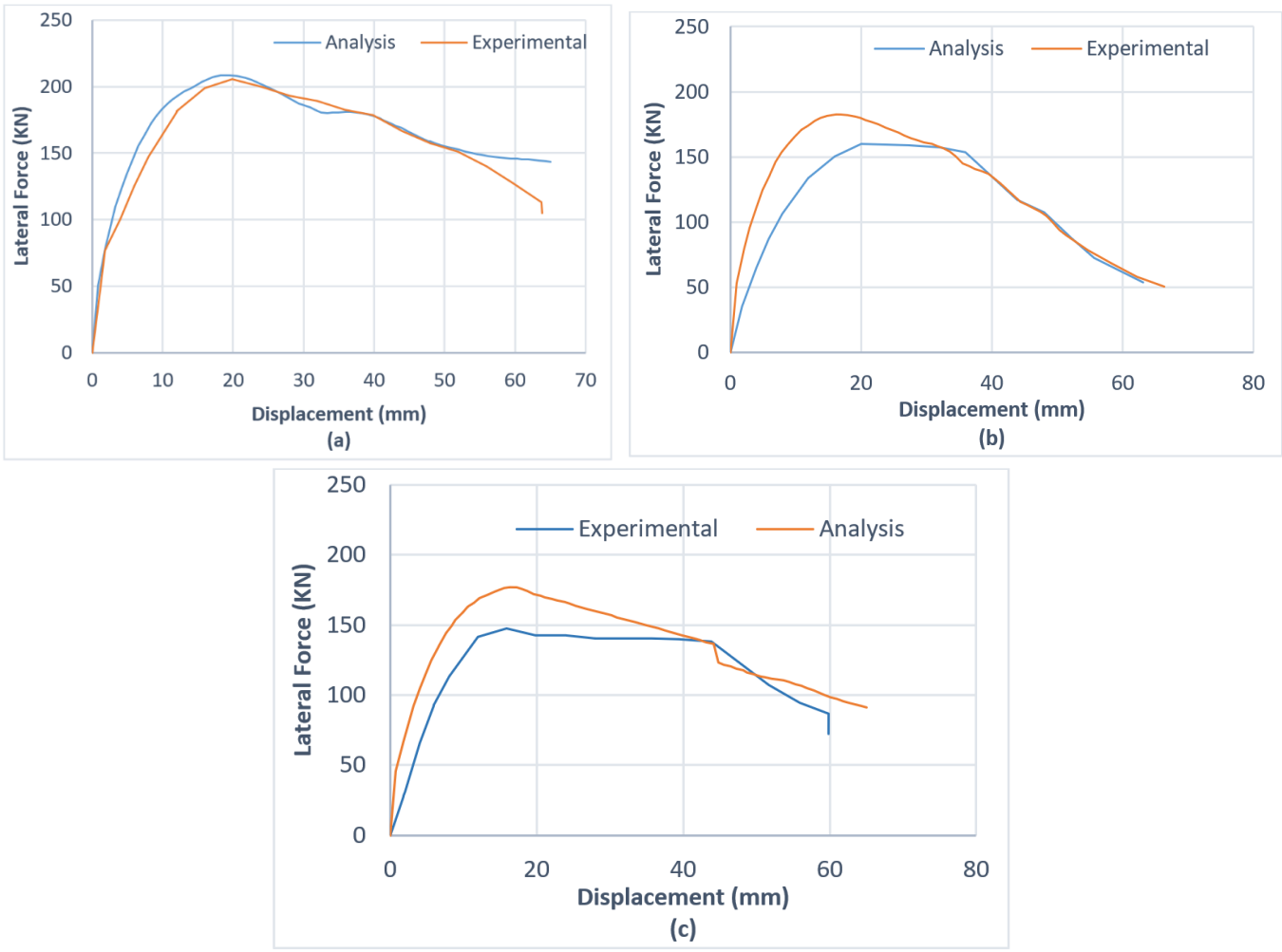

Figure 19. Comparing the backbone diagram experiment findings with the FE analysis results for DRAC, Box70, and L50 (a, b, and c)

5. CONCLUSION

This study provides a comprehensive evaluation of the seismic performance of three different coupling beam configurations—DRAC, Box70, and L50—through both experimental testing and finite element analysis. A key contribution of this research lies in the introduction of optimized diagonal reinforcement in the DRAC specimen, which significantly enhanced structural performance under cyclic loading. Unlike traditional reinforcement methods, the proposed design effectively improved crack resistance, energy dissipation, and lateral load-bearing capacity. The L50 specimen, incorporating L-shaped steel reinforcement, exhibited a balanced response with enhanced ductility, while the Box70 specimen, lacking concrete infill, demonstrated limited structural integrity, experiencing rapid stiffness degradation and extensive cracking. The finite element models developed using ABAQUS/CAE 2022 successfully captured the load response characteristics of the specimens, confirming the validity of the experimental results and providing a reliable predictive tool for further structural optimizations.

All specimens exhibited shear and flexural failure modes, but their crack progression varied. The DRAC specimen showed 20% better crack resistance. The L50 specimen exhibited a balanced crack distribution with 15% improved energy absorption over Box70, while Box70 experienced rapid cracking and spalling due to the absence of concrete infill.

The L50 specimen exhibited the highest ductility coefficient of 4.75, surpassing DRAC (3.03) by 36% and Box70 (2.83) by 68%, due to its L-shaped steel reinforcement, which effectively resisted deformation while maintaining energy dissipation capabilities, making it a viable option where deformation capacity is prioritized.

To advance the understanding and practical application of the Equivalent Diagonal Reinforcement (EDR) system, future investigations should include full-scale experimental tests on EDR-integrated coupling beams subjected to multi-directional cyclic loads to replicate realistic seismic effects, including torsional demand. Moreover, parametric finite element studies are recommended to evaluate the sensitivity of the EDR system to key design variables such as diagonal angle, steel profile thickness, anchorage detailing, and confinement level. A comparative performance study incorporating hybrid reinforcement layouts (EDR combined with Fiber Reinforced Polymers or Ultra-High-Performance Concrete in the beam core) could reveal synergistic enhancements in ductility and damage control. Finally, extending the study to frame-wall systems incorporating EDR across multiple stories would offer insights into system-level seismic interaction, enabling the development of EDR design provisions suitable for inclusion in seismic design codes.

While the experimental investigation qualitatively illustrated the evolution of crack patterns and damage states across all specimens (Figures 10–12), a quantitative analysis

of crack width propagation was not initially provided. To address this, future work will incorporate high-resolution Digital Image Correlation (DIC) or linear crack-width gauges at critical locations to capture the temporal evolution of crack openings during each loading cycle.

REFERENCES

[1] Abdelwahed, B. (2019). A review on building progressive collapse, survey and discussion. Case Studies in Construction Materials, 11: e00264. https://doi.org/10.1016/j.cscm.2019.e00264

[2] Zhang, Q., Luo, Z., Chen, Y., Wang, Z. (2023). Physical model experiments on failure mechanism on slopes of weathered basalt soils during heavy rainfall events. Materials, 16(2): 832. https://doi.org/10.3390/ma16020832

[3] El-Tawil, S., Kuenzli, C., Hassan, M., Kunnath, S. (2000). Inelastic behavior of hybrid coupled walls. In Composite Construction in Steel and Concrete IV, pp. 959-970. https://doi.org/10.1061/40616(281)83

[4] Aristizabal-Ocfaoa, J.D. (1987). Seismic behavior of slender coupled wall systems. Journal of Structural Engineering, 113(10): 2221-2234. https://doi.org/10.1061/(ASCE)0733-9445(1987)113:10(2221)

[5] Chetchotisak, P., Teerawong, J., Hansapinyo, C. (2024). Strut-and-tie model including shear–flexure interaction for predicting shear capacity of reinforced concrete short coupling beams. Structures, 66: 106791. https://doi.org/10.1016/j.istruc.2024.106791

[6] Tian, J., Zhao, Y., Tian, P., Ren, W., Li, Z., Mu, L., Lu, J. (2023). Seismic behaviour of plate-reinforced composite coupling beams with RC slabs. Soil Dynamics and Earthquake Engineering, 171: 107984. https://doi.org/10.1016/j.soildyn.2023.107984

[7] Bagheri, M.M., Doudak, G. (2021). Experimental and numerical study on the deflection of multi-storey light-frame timber shear walls. Engineering Structures, 233: 111951. https://doi.org/10.1016/j.engstruct.2021.111951

[8] Tian, J., Zhao, Y., Wang, Y., Liu, J., Du, N., Jian, Z., Yuan, Z. (2023). Seismic performance and numerical analysis of steel plate-fiber reinforced concrete composite coupling beams. Structures, 48: 258-274. https://doi.org/10.1016/j.istruc.2022.12.094

[9] Harries, K.A. (2001). Ductility and deformability of coupling beams in reinforced concrete coupled walls. Earthquake Spectra, 17(3): 457-478. https://doi.org/10.1193/1.1586184

[10] Park, W.S., Kang, T.H.K., Kim, S., Yun, H.D. (2020). Seismic performance of moderately short concrete coupling beams with various reinforcements. ACI Structural Journal, 117(3): 141-154. https://doi.org/10.14359/51723501

[11] Harries, K.A., Mitchell, D., Cook, W.D., Redwood, R.G. (1993). Seismic response of steel beams coupling concrete walls. Journal of Structural Engineering, 119(12): 3611-3629. https://doi.org/10.1061/(ASCE)0733-9445(1993)119:12(3611)

[12] Ramos, L., Hube, M.A. (2021). Seismic response of reinforced concrete wall buildings with nonlinear coupling slabs. Engineering Structures, 234: 111888. https://doi.org/10.1016/j.engstruct.2021.111888

[13] Ji, X., Wang, Y., Zhang, J., Okazaki, T. (2017). Seismic behavior and fragility curves of replaceable steel coupling beams with slabs. Engineering Structures, 150: 622-635. https://doi.org/10.1016/j.engstruct.2017.07.045

[14] Vargas, R., Bruneau, M. (2009). Experimental response of buildings designed with metallic structural fuses. II. Journal of Structural Engineering, 135(4): 394-403. https://doi.org/10.1061/(ASCE)0733-9445(2009)135:4(394)

[15] Hu, X.W., Ding, R., Zhang, Z.Y., Fan, J.S. (2024). Numerical study on optimized application of engineered cementitious composites in RC coupled shear wall structures. Journal of Building Engineering, 86: 108869. https://doi.org/10.1016/j.jobe.2024.108869

[16] Li, S., Jiang, H., Kunnath, S.K. (2023). Seismic assessment of a new resilient coupled shear wall. Engineering Structures, 277: 115476. https://doi.org/10.1016/j.engstruct.2022.115476

[17] Fortney, P.J., Shahrooz, B.M., Rassati, G.A. (2007). Large-scale testing of a replaceable "fuse" steel coupling beam. Journal of Structural Engineering, 133(12): 1801-1807. https://doi.org/10.1061/(ASCE)0733-9445(2007)133:12(1801)

[18] Li, X., Lv, H. L., Zhang, G.C., Ding, B.D. (2015). Seismic behavior of replaceable steel truss coupling beams with buckling restrained webs. Journal of Constructional Steel Research, 104: 167-176. https://doi.org/10.1016/j.jcsr.2014.09.017

[19] Zhao, Y., Dong, Y. (2020). Seismic response of reinforced concrete frame-shear wall structure with metal rubber-based damper in coupling beam. Annales de Chimie Science des Matériaux, 44(5): 319-326. https://doi.org/10.18280/acsm.440503

[20] Zhao, Y., Zhang, L. (2020). Damage quantification of frame-shear wall structure with metal rubber dampers under seismic load. Journal of Composite & Advanced Materials-Revue des Composites et des Matériaux Avancés, 30(5-6): 227-234. https://doi.org/10.18280/rcma.305-605

[21] Qiang, H., Feng, P., Stojadinovic, B., Lin, H., Ye, L. (2019). Cyclic loading behaviors of novel RC beams with kinked rebar configuration. Engineering Structures, 200: 109689. https://doi.org/10.1016/j.engstruct.2019.109689

[22] Zhao, Y., Liu, B., Li, H., Liu, H., Zhou, G. (2021). Hysteretic stressing state features of RCB shear walls revealed by structural stressing state theory. Case Studies in Construction Materials, 15: e00674. https://doi.org/10.1016/j.cscm.2021.e00674

[23] Nordin, N., Afandi, M.Z.H.Z. (2023). Finite element analysis of reinforced concrete beam-column connection with kinked rebar configuration under lateral cyclic loading using Abaqus. International Journal of Infrastructure Research and Management, 11(1): 11-24.

[24] Ji, X., Wang, Y., Ma, Q., Okazaki, T. (2017). Cyclic behavior of replaceable steel coupling beams. Journal of Structural Engineering, 143(2): 04016169. https://doi.org/10.1061/(ASCE)ST.1943-541X.0001661

[25] Sarhan, M.M. (2019). Flexural behaviour of concrete beams reinforced with steel plates. Doctoral dissertation, University of Wollongong.

[26] Yu, Q., Wu, H., Li, L., Ogail, E., Liu, Q., Zhao, X., Liu,

Y. (2023). Seismic performance analysis and evaluation of tall structures using grille-type steel plate composite shear walls. The Structural Design of Tall and Special Buildings, 32(13): e2037. https://doi.org/10.1002/tal.2037
[27] Zhai, X., Zha, X., Chen, D. (2023). Shaking table tests on 0.5-scale multistory models of plate-type modular steel and composite buildings with semi-rigid corner connections. Thin-Walled Structures, 188: 110833. https://doi.org/10.1016/j.tws.2023.110833
[28] Chan-Anan, W., Leelataviwat, S., Goel, S.C. (2016). Performance-based plastic design method for tall hybrid coupled walls. The Structural Design of Tall and Special Buildings, 25(14): 681-699. https://doi.org/10.1002/tal.1278
[29] Jiang, H., Li, S., Bolander, J.E., Kunnath, S.K. (2023). Seismic performance of a new type of coupled shear wall with replaceable components: Experimental validation. Journal of Earthquake Engineering, 27(4): 810-832. https://doi.org/10.1080/13632469.2022.2033353
[30] Wani, Z.R., Tantray, M., Farsangi, E.N. (2022). In-plane measurements using a novel streamed digital image correlation for shake table test of steel structures controlled with MR dampers. Engineering Structures, 256: 113998. https://doi.org/10.1016/j.engstruct.2022.113998
[31] Rashid, Z., Tantray, M., Noroozinejad Farsangi, E. (2022). Acceleration response-based adaptive strategy for vibration control and location optimization of magnetorheological dampers in multistoried structures. Practice Periodical on Structural Design and Construction, 27(1): 04021065. https://doi.org/10.1061/(ASCE)SC.1943-5576.0000648
[32] ACI Committee 318. (2022). ACI CODE-318-19(22): Building Code Requirements for Structural Concrete and Commentary (Reapproved 2022). American Concrete Institute.
[33] Wang, B., Jiang, H., Lu, X. (2017). Experimental and numerical investigations on seismic behavior of steel truss reinforced concrete core walls. Engineering Structures, 140: 164-176. https://doi.org/10.1016/j.engstruct.2017.02.055
[34] Benam, M.B., Azar, B.F., Veladi, H. (2022). Experimental and numerical analyses of seismic behavior of concrete shear wall with opening accompanied by steel frame and eccentric encased steel braces. Engineering Structures, 256: 113989. https://doi.org/10.1016/j.engstruct.2022.113989
[35] Nie, J., Qin, K., Cai, C.S. (2008). Seismic behavior of connections composed of CFSSTCs and steel–concrete composite beams—experimental study. Journal of Constructional Steel Research, 64(10): 1178-1191. https://doi.org/10.1016/j.jcsr.2007.12.004
[36] Wang, M.F., Luo, D., Hu, Z.Q. (2020). Seismic performance of steel-enhanced damping concrete core walls with concealed steel plate bracings. Engineering Structures, 213: 110564. https://doi.org/10.1016/j.engstruct.2020.110564
[37] Dong, Y.R., Xu, Z.D., Zeng, K., Cheng, Y., Xu, C. (2018). Seismic behavior and cross-scale refinement model of damage evolution for RC shear walls. Engineering Structures, 167: 13-25. https://doi.org/10.1016/j.engstruct.2018.03.096
[38] Birtel, V.A.M.P., Mark, P. (2006). Parameterised finite element modelling of RC beam shear failure. In ABAQUS Users' Conference (Vol. 14).
[39] Abaqus, G. (2011). Abaqus 6.11. Dassault Systemes Simulia Corporation, Providence, RI, USA, 3: 73.